# Roles of impurities on precipitation kinetics of dilute Al–Sc alloys

Ofer Beeri [a,*], David C. Dunand [a], David N. Seidman [a,b]

[a] Department of Materials Science and Engineering, Northwestern University Evanston, IL 60208-3108, USA
[b] Northwestern University Center of Atom-Probe Tomography (NUCAPT), Evanston, IL 60208-3108 USA

## ARTICLE INFO

## ABSTRACT

High-purity (HP) aluminum and commercial purity (CP) aluminum (major impurities: ~250 at. ppm Si and ~130 at. ppm Fe) are alloyed with ~250 to ~1100 at. ppm Sc and ~50 at. ppm RE (RE = La, Ce, Pr, or Nd). The alloys are homogenized at 640 °C and aged at 300 °C. The precipitation kinetics, basic mechanical properties, and microstructure are studied using AC electrical conductivity, microhardness measurements, scanning electron microscopy in conjunction with energy dispersive X-ray spectroscopy, and atom-probe tomography, respectively. The Fe and RE elements form micrometer-scale diameter $Al_{\sim3}(Fe,RE)$ primary precipitates, which have no effect on the mechanical properties. Silicon accelerates the precipitation kinetics of nanometer-scale diameter $Al_3Sc$ precipitates, increasing their number density, thereby resulting in higher microhardness values for CP aluminum than the HP aluminum having the same Sc concentration. Additionally, the Sc equilibrium solubility in the $\alpha$-Al matrix is estimated and Orowan's strengthening mechanism is confirmed for the $Al_3Sc$ precipitates.

## 1. Introduction

Scandium is the most effective alloying element for precipitation strengthening of Al alloys on a per atom basis [1]. Hence, there is a significant extant literature on the strengthening effects of Sc in Al alloys, which results from the precipitation of nanosize coherent $Al_3Sc$ ($L1_2$ structure) precipitates with a small lattice parameter mismatch with the $\alpha$-Al matrix [2]. At ambient temperature the lattice parameters of Al and $Al_3Sc$ are 0.4049 and 0.4103 nm, respectively [3,4], resulting in an unrelaxed lattice parameter mismatch of 1.34%, while at 300 °C, due to thermal expansion, this mismatch decreases to about 1.1% [5].

There is considerable research on Al alloys containing Sc, focusing on commercial alloys (containing many alloying elements and impurities) with additions of relatively high Sc concentrations, typically 0.12–0.24 at.% Sc (0.2–0.4 wt.%); the maximum solubility of Sc in $\alpha$-Al is 0.38 at.% at the eutectic temperature (660.0 °C). Additionally, researchers have investigated high-purity (HP) Al with additions of 0.06–0.24 at.% Sc (0.1–0.4 wt.%) and one or two additional alloying elements (for instance, X = Ti, Zr or rare earths (REs) [6–10]), added to replace Sc in $Al_3(Sc_{1-x}X_x)$ precipitates, thereby utilizing a less expensive element than Sc, while maintaining or even enhancing the mechanical properties at ambient and elevated temperatures. The role of impurities in nucleating precipitates in Al alloys is well known [11]. There is, however, no systematic study, to the best of our knowledge, of the effects of specific impurities on the nucleation, growth and coarsening of $Al_3Sc$ precipitates in $\alpha$-Al.

In this article we present the results of a study that characterizes the effects of the common impurities Fe and Si, on the ageing behavior of Al alloyed with a small concentration of Sc [<0.11 at.% (<0.18 wt.%)]. An additional and related goal is to study the effect of replacing some of the Sc in $Al_3Sc$ with REs, added at concentrations comparable to those of the Fe or Si impurities.

## 2. Experimental procedures

All alloys were cast using master alloys and pure Al. The Al–Si, Al–Fe and Al–RE [RE = La, Ce, Pr, Nd or mischmetal (MM)] master alloys were processed by arc melting commercial purity Al (CP-Al, see details below) and 99.99% pure Fe, 99.99% Si and 99.99% RE (except Ce, which has a purity of 99.9%) under an argon atmosphere; the MM composition is 23 at.% La, 55 at.% Ce, 5 at.% Pr, 17 at.% Nd. A commercial master Al–1.2 at.% Sc (2 wt.%) alloy was used (Ashurst Inc.) as the source of Sc. Two sources of Al were utilized, high-purity Al (HP-Al) and CP-Al. Their chemical compositions are presented in Table 1.

For each alloy, the proper weights of master alloys and pure aluminum were melted at 775 °C in a resistance heated furnace in an atmosphere of air using an alumina crucible coated with zirconia. To minimize oxidation of the alloying elements, the CP-Al or HP-Al was first melted before adding the master alloy wrapped in Al

**Table 1**
A listing of the results of the chemical analyses of the two sources of the different aluminum (not including gaseous elements) samples, where only elements with a concentration greater than 1 wt. ppm are listed.

| Element | HP-Al at. ppm (wt. ppm) | CP-Al at. ppm (wt. ppm) |
|---|---|---|
| Be | 6 (2) | <0.01 (<0.005) |
| B | 7 (3) | 3 (1) |
| Mg | 4 (4) | 4 (4) |
| Si | 38 (40) | 259 (270) |
| P | 3 (3) | 0.3 (0.3) |
| Ti | 1 (2) | 13 (23) |
| V | 4 (7) | 20 (37) |
| Cr | 1 (2) | 2 (3) |
| Mn | 3 (7) | 3 (6) |
| Fe | 24 (49) | 126–256 (260–530)[a] |
| Ni | 0.5 (1) | 11 (23) |
| Cu | 18 (42) | 1 (2) |
| Zn | 2 (6) | 33 (80) |
| Ga | 3 (9) | 33 (84) |
| Zr | 0.3 (1) | 2 (8) |
| Mo | 0.8 (3) | 0.6 (2) |
| Pb | 0.9 (7) | 0.7 (5) |
| Total | 118 (188) | 510–640 (808–1078) |

[a] The concentrations in CP-Al are nonuniform and in some cases the Fe concentration is found to be 256 at. ppm, while in other cases it is found to be 126 at. ppm.

foil (99.99% pure). The melt was then stirred with an alumina rod to ensure homogeneity, and cast in a graphite mold in the shape of four rods, each of which was about 12 mm in diameter and 100 mm in length. The mold was placed on a massive Cu platen to guarantee directional solidification.

Cylinders 4–5 mm in height were cut from the rods, which were placed in a resistance heated air furnace at 640 °C for 5–7 days to ensure full homogenization, and then water-quenched to room temperature. To verify the compositions and to ensure uniformity two samples were chemically analyzed from each casting, one from the top and one from the bottom of each rod. The compositions of all the alloys are displayed in Table 2. The ageing treatments were performed at 300 °C for times up to 1 month, and terminated by water quenching to room temperature.

Electrical conductivity measurements of the samples were performed at room temperature with an eddy-current tester (Sigmatest model 2.069, Foerster Instruments, Pittsburgh, PA), calibrated prior to each measurement against several standards having known electrical conductivities in the range 4–40 MS m$^{-1}$. We typically used a frequency of 60 kHz, for which the results are not sensitive to surface roughness; that is, polished and as-cut samples yielded the same results. The Vickers microhardnesses of the samples (mounted and mechanically polished to 1 μm) were measured under a load of 200 g for 5 s. The reported values are an average of ten different measurements performed on the same sample in different locations. Selected samples, electropolished and electro-etched, were inspected both metallographically and by a JEOL JSM 5600 scanning electron microscope (SEM), equipped with an energy dispersive spectrometer (EDS). Sample preparation methods for study by local-electrode atom-probe (LEAP) tomography are described elsewhere [6], which includes mechanical cutting, grinding, and electropolishing. The samples were loaded into an Imago Scientific Instruments LEAP-3000 tomograph in less than a few hours after electropolishing. Measurements were performed at a specimen temperature of 30 K using the electrical pulsing mode at a pulse repetition rate of 200 kHz and a pulse fraction (ratio of pulse voltage to steady-state dc voltage) of 20%. The three-dimensional reconstructions were performed using Imago's IVAS program (versions 2.3.1, 3.0a1, and 3.0a2).

## 3. Experimental results

### 3.1. Precipitate morphologies

Fig. 1 displays some characteristic morphologies of precipitates found in samples processed using CP-Al with different levels of REs and different heat treatments (see caption for Fig. 1 for details). Some of the precipitates were distributed within grains (Fig. 1(a) and (c)) and some were located at grain boundaries (GBs), Fig. 1(b), (d) and (e). These precipitates are primary precipitates nucleated during solidification and they can be seen in the as-cast samples (not presented in Fig. 1), as well as in the homogenized and in the aged samples. The chemical compositions of the precipitates were measured using EDS in a SEM yielding Al$_3$(Fe,RE). The ratio Fe:RE is always approximately the same as the nominal Fe:RE ratio in a sample; that is, between 3:1 for the smaller Fe concentration samples and 5:1 for the larger Fe concentration samples, Tables 1 and 2. This result demonstrates that the RE elements are scavenged by the Al$_3$Fe precipitates. Moreover, for samples containing MM, the ratio between the different RE elements in the precipitates is approximately the same as their ratio in the source MM alloy, suggesting equal scavenging efficiency for the four different RE elements (La, Ce, Pr, Nd) present in MM. A result of this scavenging effect is that the RE concentration in the CP-Al matrix is smaller than the initial
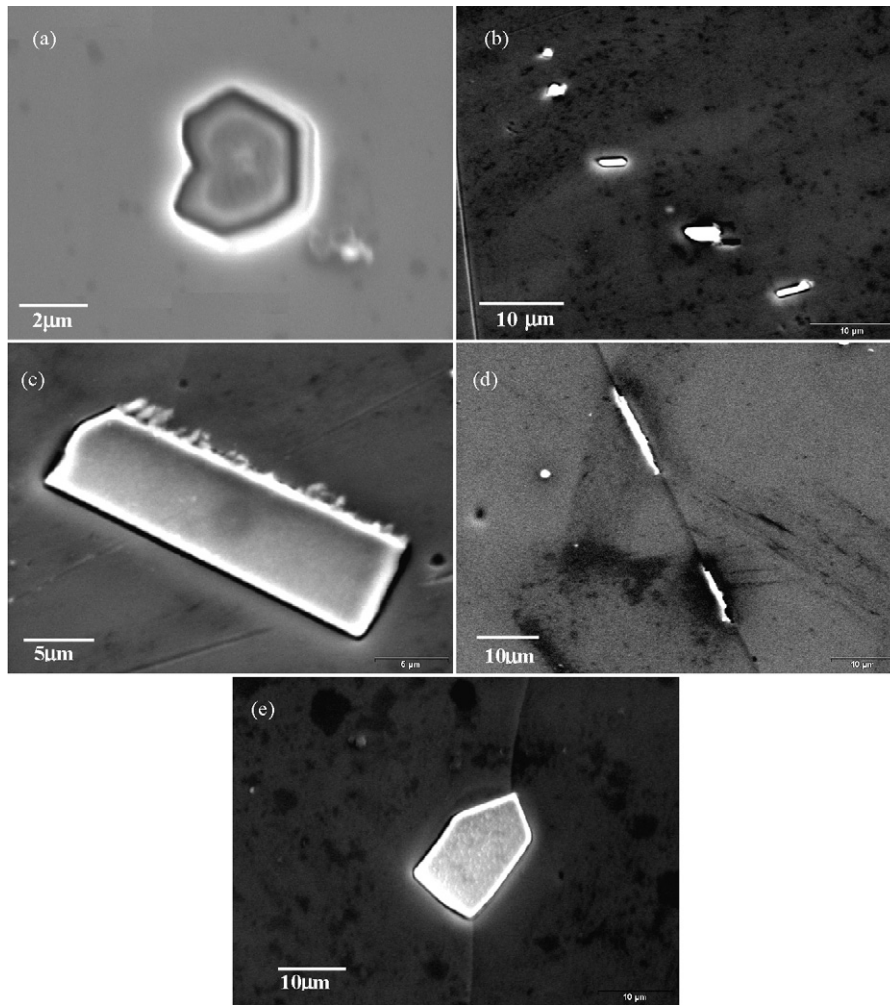
**Table 2**
Chemical compositions of the different Al alloy samples.

| Alloy no. | Source Al | Sc (at. ppm) | RE (at. ppm) | Fe[a] (at. ppm) | Si[a] (at. ppm) |
|---|---|---|---|---|---|
| 1. | CP | 636 | 45 La | | |
| 2. | CP | 713 | 54 Ce | | |
| 3. | CP | 1085 | 45 Pr | | |
| 4. | CP | 285 | 40 Nd | | |
| 5. | CP | 980 | 58 MM | | |
| 6. | CP | 276 | 41 La | | |
| 7. | CP | 324 | 52 Ce | | |
| 8. | CP | 324 | 46 Pr | | |
| 9. | CP | 300 | 41 Nd | | |
| 10. | CP | 306 | 50 MM | | |
| 11. | CP | 306 | – | | |
| 12. | CP | 375 | – | | |
| 13. | CP | 228 | – | | |
| 14. | CP | 462 | – | | |
| 15. | HP | 252 | – | | |
| 16. | HP | 555 | – | | |
| 17. | HP | 630 | – | 289 | 270 |
| 18. | HP | 588 | – | 193 | 270 |
| 19. | HP | 618 | – | 39 | 289 |

[a] In all cases where Fe and Si are not listed, their concentration is the same as in the source Al.

**Fig. 1.** Scanning electron microscope micrographs exhibiting the different precipitate morphologies of Al$_{~3}$(Fe,RE) in samples processed using CP-Al. All samples were homogenized at 640 °C for 5–7 days. (a) CP-Al containing ~180 at. ppm Fe and ~50 at. ppm La after ageing for $1.98 \times 10^4$ s (5.5 h) at 300 °C; (b and c) CP-Al containing ~250 at. ppm Fe and ~50 at. ppm mischmetal (MM) after ageing for $1.73 \times 10^5$ s (48 h) at 300 °C; and (d and e) unaged CP-Al containing ~250 at. ppm Fe and ~50 at. ppm MM.

value of 50 at. ppm, and thus the RE effect on Al$_3$Sc precipitation is negligible.

### 3.2. Electrical conductivity measurements

The electrical conductivity versus Sc concentration is displayed in Fig. 2 for the as-homogenized samples. In the homogenized state, most of the impurities are dissolved in the α-Al matrix, hence decreasing a sample's room temperature electrical conductivity. The electrical conductivity differences between the alloys HP-Al and CP-Al are clearly seen. For the same Sc concentration, the alloys processed using HP-Al have a greater electrical conductivity because they have smaller impurity concentrations. For alloys processed using the same source of Al, the electrical conductivity of the as-homogenized samples is inversely proportional to the Sc concentration with a proportionality coefficient of about $-39.2 \pm 0.3$ MS m$^{-1}$ at.% Sc$^{-1}$. This linear dependence between Sc concentration and electrical conductivity is discussed elsewhere [12,13]. The proportionality coefficient is $-29.4$ MS m$^{-1}$ at.% Sc$^{-1}$ [12] at 77 K using HP-Al alloyed with Sc. The difference between this 77 K value [12] and the value we measured is explicable in terms of differences in the initial Al purity and the temperature at which the electrical conductivity was measured.

At 29 K the electrical conductivity of HP-Al is 37.7 MS m$^{-1}$ [14]. Extrapolating the straight lines obtained for CP-Al and HP-
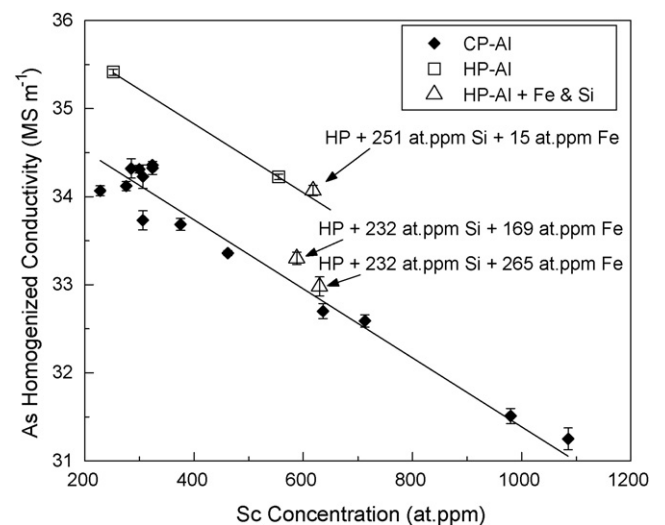


**Fig. 2.** The as-homogenized electrical conductivity versus Sc concentration (at. ppm). Two families of approximately straight lines are observed: one for the alloys processed using HP-Al; and one for the alloys processed using CP-Al. For each family the as-homogenized electrical conductivity is inversely proportional to the Sc concentration. The triangles are for data for alloys processed using HP-Al, with additions of Fe and Si.
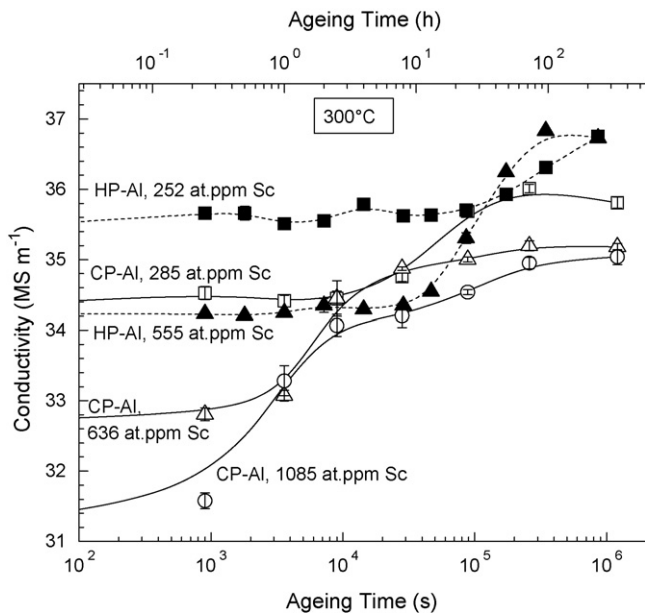
**Fig. 3.** Examples of electrical conductivity curves versus ageing time at 300 °C. The upward deviation of the curves from the homogenized value indicates the initiation of precipitation. The precipitation starting time, for the same alloy family (HP-Al or CP-Al), decreases with increasing Sc concentration.



**Fig. 4.** Examples of Vickers microhardness versus ageing time at 300 °C (the lines are a guide to the eye).

Al in Fig. 2 to zero Sc concentration yields $35.3 \pm 0.2$ MS m$^{-1}$ and $36.4 \pm 0.2$ MS m$^{-1}$, respectively, at 293 K. The difference between the extrapolated and the pure Al values is due to the presence of other impurities (totaling ~1000 at. ppm for CP-Al and ~200 at. ppm for HP-Al). This is also the reason for the higher deviation of the value obtained for the CP-Al, having a larger total impurity concentration than the HP-Al.

As indicated in Fig. 2, we also prepared and studied three alloys fabricated from HP-Al with Fe and Si additions. All three Al alloys have about 250 at. ppm Si (same as for the CP-Al), but the Fe concentration varies between about 50 and 300 at. ppm (the CP-Al alloys have ~130–250 at. ppm Fe): see discussion below.

The electrical conductivity as a function of ageing time at 300 °C is displayed in Fig. 3 for the three CP-Al and two HP-Al alloys with different Sc concentrations. The precipitation kinetics increase with increasing Sc concentration; for the same Sc concentration, the kinetics are faster for the CP-Al alloys. For instance, HP-Al with 252 at. ppm Sc has not achieved its peak electrical conductivity (corresponding to complete precipitation of all the elements in solid solution) after $8.64 \times 10^5$ s (10 days) of aging, while CP-Al with 285 at. ppm Sc achieves its peak electrical conductivity aging value after about $2.59 \times 10^5$ s (3 days).

### 3.3. Microhardness measurements

Fig. 4 displays Vickers microhardness values (expressed in MPa using a conversion factor of 9.8) versus ageing time at 300 °C for the same alloys whose electrical conductivity results are presented in Fig. 3. For a given Sc concentration, the microhardness values of the CP-Al alloys are greater than that of the HP-Al alloys. This difference is significant; for example, the peak microhardness value of the CP-Al alloy, containing 285 at. ppm Sc, is greater than that of the HP-Al alloy containing almost 1.95 times as much Sc (555 at. ppm). Additionally, over-ageing is exhibited by the CP-Al alloys with the largest Sc concentration, 1085 at. ppm. This is attributed to a decrease in the precipitate number density, $N_v$, as a result of both growth and coarsening.
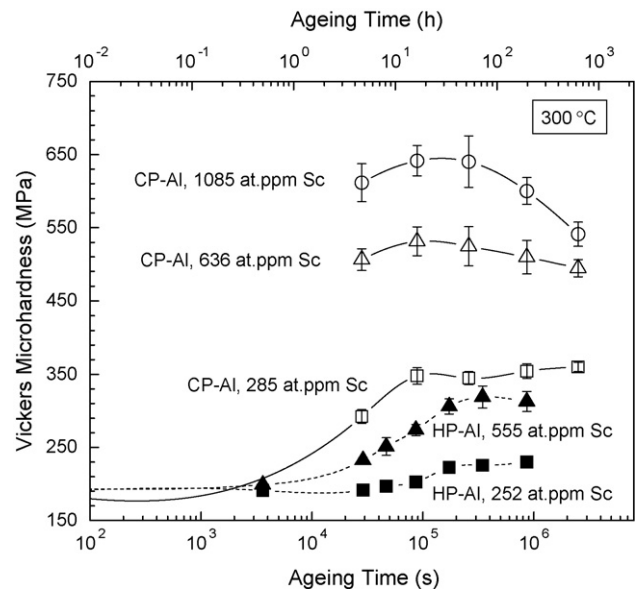
Fig. 5 displays the peak microhardness of each alloy versus its Sc concentration. Again, the differences between the two families of samples are clear, with the CP-Al alloys having larger microhardness values and the HP-Al alloys having smaller microhardness values for a given Sc concentration. For each family of curves, the peak microhardness values increase with increasing Sc concentration. The three HP-Al alloys, with additions of Si and Fe, fall on the same curve as the CP-Al alloys. These three HP-Al alloys contain about 280 at. ppm Si, with Fe additions of 15, 169 or 265 at. ppm. The results for these Si and Fe concentrations and the microhardness values suggest strongly that the source of the larger microhardness values of the CP-Al alloys, with respect to the HP-Al alloys, is the larger Si concentration in these alloys.

### 3.4. 3D Local-electrode atom-probe (LEAP) tomographic results

Fig. 6 displays representative reconstructions of the LEAP tomographic measurements of the CP-Al alloys. It includes examples for
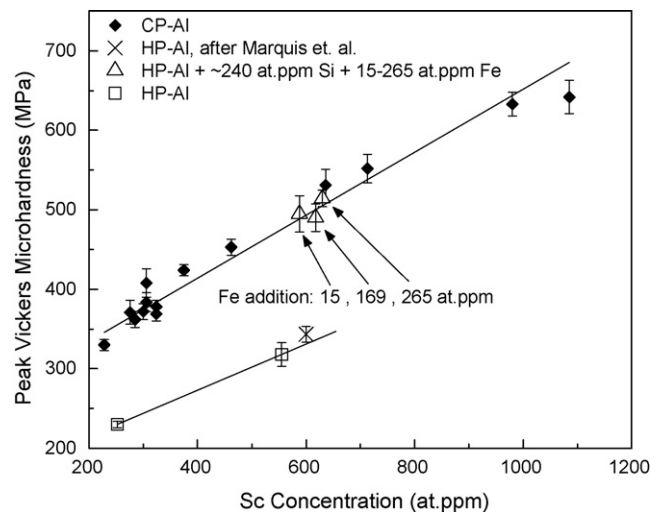


**Fig. 5.** Peak Vickers microhardness values versus Sc concentration (at. ppm) for all alloys studied. The data point represented by a cross is a result for an Al–Sc binary (600 at. ppm Sc) [19]. The lines are linear least-squares fits to the data points.
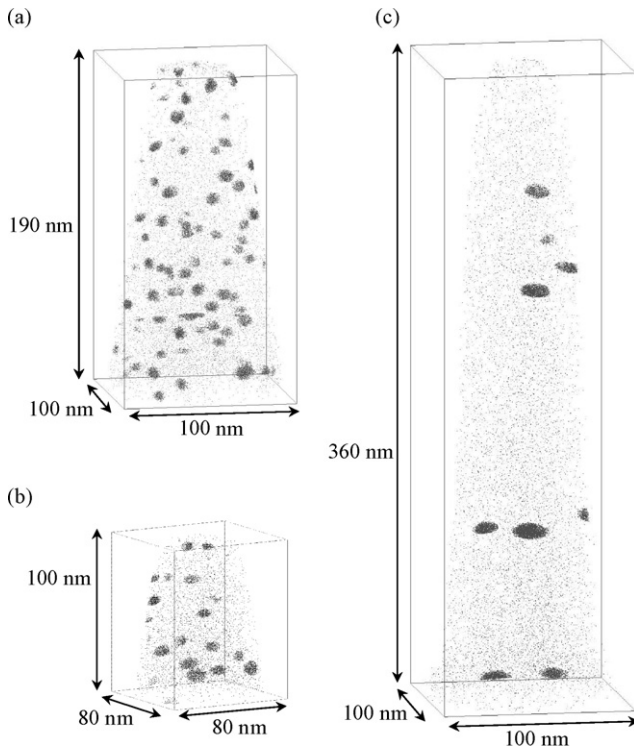
**Fig. 6.** Representative LEAP tomographic reconstructions from CP-Al aged at 300 °C. The dots represent Sc atoms and the Al atoms are omitted for clarity. (a) Alloy containing 980 at. ppm Sc and 58 at. ppm mischmetal (MM), representing large Sc concentration alloys, aged for $2.59 \times 10^5$ s (72 h), the dataset contains $28 \times 10^6$ atoms and 73 precipitates, the elongated shape of the precipitates is a reconstruction artifact due to the elliptical cross-section of this tip; (b) Alloy containing 636 at. ppm Sc and 45 at. ppm La (representing the intermediate Sc concentration alloys) aged for $2.59 \times 10^5$ s (72 h), the dataset contains $9 \times 10^6$ atoms and 17 precipitates; and (c) Alloy containing 306 at. ppm Sc and no RE (representing small Sc concentration alloys), aged for $9 \times 10^4$ s (25 h), the dataset contains $52 \times 10^6$ atoms and 9 precipitates.
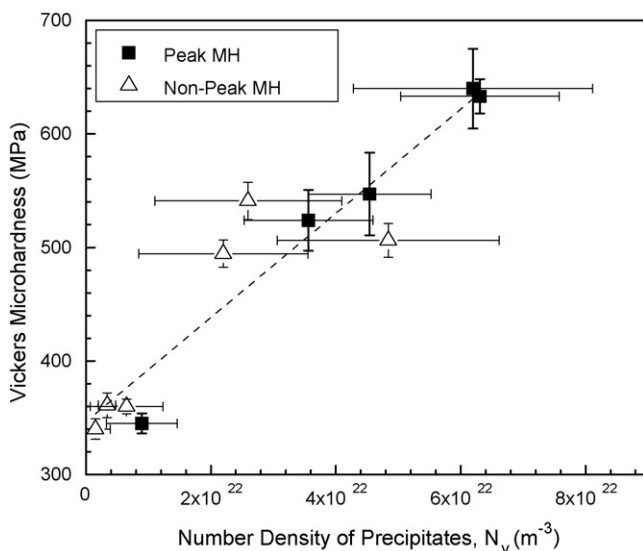


**Fig. 7.** Microhardness values versus precipitate number density, $N_v$, for the CP-Al alloys aged to peak microhardness (solid squares) and before reaching peak microhardness (open triangles). The error bars for $N_v$ are the statistical error associated with counting statistics. The peak microhardness error bars are the standard deviations of the microhardness measurements.
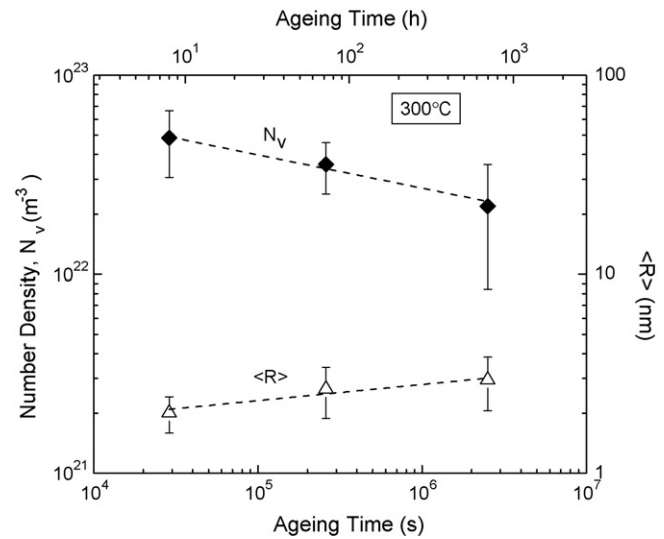


**Fig. 8.** Average precipitate radius, $\langle R \rangle$, and number density, $N_v$, versus ageing time at 300 °C for the CP-Al alloy containing 636 at. ppm Sc. The error bars are for the counting statistics errors: see text for details.

alloys with: (a) a large Sc concentration, 980 at. ppm, Fig. 6(a); (b) an intermediate Sc concentration, 636 at. ppm, Fig. 6(b); and (c) a small Sc concentration, 306 at. ppm Sc, Fig. 6(c). For the smallest Sc concentration (a data set of 52 million atoms), Fig. 6(c), there are 9 precipitates, and hence evaluating the precipitate number density, $N_v$, from the LEAP tomographic data involves a statistical error of about 40%. No LEAP tomographic evaluations were performed for the HP-Al alloys, since the $N_v$ values were estimated to be even smaller based on their small microhardness values. For the large Sc concentration alloys, where N$_v$ is greatest ($6.3 \times 10^{22}$ m$^{-3}$), its evaluation, and other precipitate properties, are more statistically reliable. The value of $N_v$ for each alloy is calculated by combining datasets from several specimens (between one to four) to improve the counting statistics. The uncertainty involved in the estimation of $N_v$, as shown in the figures, calculated using counting statistics, taking into account the uncertainties in the evaluation of the number of atoms and the number of precipitates in the sampled volume. There is an approximately linear relationship between the microhardness of the CP-Al alloys and their $N_v$ values (Fig. 7). This linear relationship is phenomenological; the detailed relationship between the microhardness and $N_v$ is given in Section 3.6. Since the peak microhardness values also increase essentially linearly with Sc concentration (Fig. 5), a linear dependence also exists between Sc concentration and the $N_v$ value at peak microhardness.

### 3.5. Growth and coarsening behavior of precipitates

To evaluate the growth and coarsening behavior of the precipitates, the following three different specimens from the same CP-Al alloy, containing 636 at. ppm Sc, are analyzed utilizing LEAP tomography: (i) one after ageing for $2.88 \times 10^4$ s (8 h); (ii) the second after ageing for $2.59 \times 10^5$ s (3 days); and (iii) the third after ageing for $2.51 \times 10^6$ s (29 days). Fig. 8 displays the slow increase of the mean precipitate radius, $\langle R \rangle$, and concomitant decrease in $N_v$ with increasing aging time: note the small increase in $\langle R \rangle$ from 2 to 3 nm in 29 days. The error bars for $\langle R \rangle$ reflect the counting statistical error, which is given by $\langle R \rangle / \sqrt{n}$, where $n$ is the number of precipitates in each dataset.

A standard way of displaying a concentration profile utilizes the proximity histogram plot (proxigram for short) [15]. Fig. 9 is a proximity histogram for the Al and Sc profiles in the CP-Al alloy containing 636 at. ppm Sc, after an ageing time of $2.59 \times 10^5$ s (3 days).
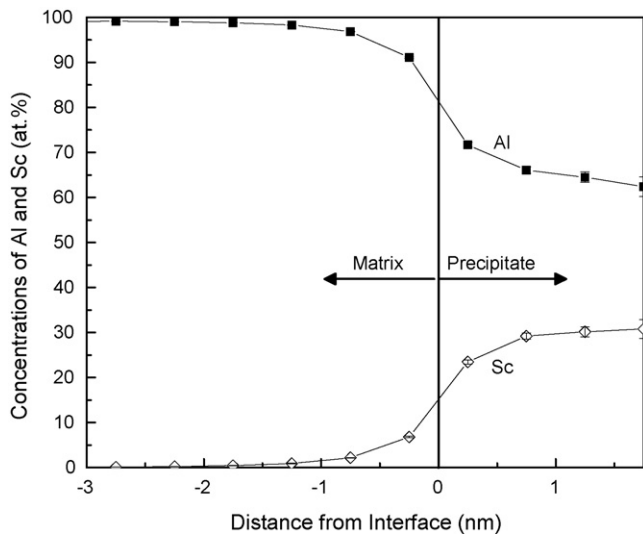
**Fig. 9.** Proxigram displaying the Al and Sc concentration profiles for the CP-Al alloy containing 636 at. ppm Sc for an ageing time of $2.59 \times 10^5$ s (72 h). The α-Al matrix/precipitate isoconcentration surface is for a Sc concentration of 15 at.%.

The isoconcentration surface chosen corresponds to a Sc concentration of 15 at.%. The exact location of the heterophase interface depends on the Sc concentration chosen for defining the isoconcentration surface; in this case, however, as long as this value is between ~1% and ~20% Sc, the general shape of the proxigram is invariant and there is only a shift of the abscissa [16]. For the precipitate concentration, the region where the Sc concentration is approximately constant is taken, while for the matrix concentration, a region about 10 nm away from the α-Al/Al₃Sc heterophase interface is employed. The calculated values include a correction for the background white noise, which is approximately 200 at. ppm. These Sc concentration values are listed in Table 3. In the Al₃Sc precipitates, the Sc concentration is about 36 at.% Sc at 8 h, while for longer ageing times (>3 days) it is almost constant at approximately 30%, which demonstrates that the Sc concentration in the precipitates is temporally evolving toward its equilibrium value. This result, where the Sc concentration is initially greater than the stoichiometric value of 25 at.% is not unique to this work [10,17,18] and we have observed this phenomenon in other alloys, for example, Al–Sc–Zr alloys [17,18].

The evaluation of the α-Al matrix's Sc concentration is associated with a statistical error of about 60–160%, due to its small value of 120–40 at. ppm Sc, respectively. The trend, however, of decreasing Sc concentration in the α-Al matrix with increasing ageing time obtains, which was anticipated. A calculation of the rate constant associated with this value is given in Section 4.

The same data analysis for the RE elements or impurity elements (that is, calculating a proxigram and evaluating the concentration in the precipitates and in the α-Al matrix) is not practical, as due to their small concentrations the statistical uncertainty is almost the same as the signal itself. Iron and Si have larger concentrations, on the order of a few hundred at. ppm, and one should be able

**Table 3**
The average Sc concentrations in the α-Al matrix and in the precipitates for the CP-Al alloy containing 636 at. ppm Sc, aged for different times, as determined by atom-probe tomography.

| Ageing time (s) | Sc concentration in the α-Al matrix (at. ppm) | Sc concentration in the precipitates (at.%) |
|---|---|---|
| $2.88 \times 10^4$ (8 h) | $119 \pm 69$ | $36.3 \pm 2.1$ |
| $2.59 \times 10^5$ (3 days) | $85 \pm 108$ | $29.5 \pm 1.8$ |
| $2.51 \times 10^6$ (29 days) | $41 \pm 65$ | $31.6 \pm 1.9$ |

to measure their concentrations by LEAP tomography, but unfortunately their peaks in the mass spectra overlap, using voltage pulsing, with the AlH peaks: the pertinent mass-to-charge state ratios, $m/n$, are $^{56}Fe^{+2} = {}^{28}Si^{+1} = ({}^{27}Al^1H)^{+1}$ and $^{28}Si^{+2} = ({}^{27}Al^1H)^{+2}$. Du et al. [19] performed, however, three-dimensional atom-probe measurements of CP-Al alloy containing ~1000 at. ppm Sc and ~500 at. ppm Si (the concentrations of the other impurities were not reported), which immediately after solidification was quenched and then aged at 300 °C for 24 h: they ignored the peak overlap effect, and reported a value of 6 at.% Si in the Al₃Sc precipitates and a very small Si concentration in the α-Al matrix, whose exact value was not reported.

### 3.6. Strengthening mechanisms

It has been shown [6,7,10,20] that the main strengthening mechanism at room temperature, in dilute Al–Sc based alloys with nanometer-scale coherent Al₃Sc precipitates, is Orowan dislocation looping, where dislocations bypass coherent precipitates due to the linear elastic stress fields associated with them.

The Orowan bypass stress $\Delta\sigma_{or}$ is given by [21]:

$$\Delta\sigma_{or} = M \frac{0.4Gb}{\pi\lambda_{e-e}} \frac{\ln(2\bar{r}/b)}{\sqrt{1-\nu}}; \quad (1)$$

where $M = 3.06$ is the orientation factor [22], $G = 24.5$ GPa is the shear modulus of Al, $\nu = 0.345$ is Poisson's ratio, $b = 0.286$ nm is the magnitude of the Burgers vector, and $\lambda_{e-e}$ is the edge-to-edge interprecipitate distance, based on a regular array of precipitates. The quantity $\lambda_{e-e}$ for a regular array of precipitates is given by [23]:

$$\lambda_{e-e} = \left[\left(\frac{\pi}{\phi}\right)^{1/2} - 2\right]\bar{r}; \quad (2)$$

where $\phi$ is the volume fraction of the precipitates, and $\bar{r} = \sqrt{2/3}\langle R\rangle$ [21].

For each analyzed sample of the CP-Al alloys we calculated the Orowan stress, $\Delta\sigma_{or}$, calculating $\phi$ from $N_\nu$ and $\langle R\rangle$ as measured by APT, using the standard relationship $\phi = 4\pi\langle R\rangle^3 N_\nu/3$, which assumes spherical precipitates These values, for the different CP-Al alloys, are plotted in Fig. 10 as a function of a specimen's yield
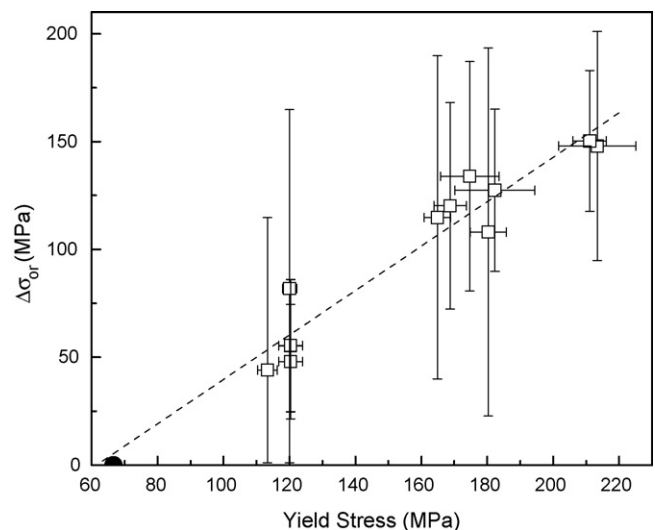


**Fig. 10.** The Orowan stress increment, $\Delta\sigma_{or}$, versus the yield stress (see text). The data are from different alloys aged for different times at 300 °C. The error bars for $\Delta\sigma_{or}$ are due to counting statistics, while the error bars for the yield stresses are the standard deviations of the microhardness measurements divided by 3. The dashed line is the least-squares best fit to a straight line. The solitary solid-black circle is a data point for the homogenized samples having a microhardness value of ~200 MPa (yield stress = ~67 MPa).

stress, which was estimated using the measured microhardness value divided by a factor of three [24]. A linear least-squares best fit yields a slope of $1.05 \pm 0.08$, confirming that the main strengthening mechanism is the Orowan mechanism for $\langle R \rangle = 2.0$–5.0 nm; the largest $\langle R \rangle$ value of 5 nm was measured after 72 h ageing of an alloy containing only 285 at. ppm Sc resulting in microhardness value of 345 MPa.

## 4. Discussion

### 4.1. Roles of impurities on precipitation

The roles of impurities on the disparate ageing kinetics of the HP-Al and CP-Al alloys are now discussed. From Figs. 2–5 it is clear that the CP-Al alloys have faster precipitation kinetics and greater Vickers microhardness values than the HP-Al alloys for the same Sc concentrations. Since the major impurities in the CP-Al alloys are Si and Fe, these elements are highly likely responsible for this difference.

The microhardness results for the three alloys processed using HP-Al with additions of Fe and Si (Fig. 5) are the same as the CP-Al alloys, implying that Si is the element responsible for the differences between the two alloys. Moreover, because Fe is present in the micrometer-scale diameter $Al_3Fe$ precipitates (Fig. 1) it is not available for affecting the precipitation kinetics of the nanometer-scale $Al_3Sc$ precipitates. This result is in agreement with published results [25–28] demonstrating that Fe has practically no effect on altering $Al_3Sc$ precipitation kinetics for the concentration range studied.

An important related result for $Al_3Fe$ precipitates is their efficient scavenging effect of RE elements that depletes their concentrations in the $\alpha$-Al matrix in about the same ratio as the Fe concentration, as evidenced by the Fe:RE ratio in these precipitates.

The influence of Si on $A_3Sc$ precipitates, namely faster precipitation kinetics and larger $N_v$ values for the same Sc concentration, is less well established in the literature. The $\alpha$-Al-rich region of the ternary Al–Sc–Si phase diagram [29] exhibits four phases: $\alpha$-Al, $Al_3Sc$ (L1$_2$), $Sc_2AlSi_2$ (V-phase, having a tetragonal structure lattice parameters, $a = 0.659$ nm and $c = 0.399$, and a $U_3Si_2$-type superstructure intermetallic compound) and Si solid solution. The latter two exist only at Si concentrations greater than the values we studied and hence do not concern us. The region of the phase diagram for small Sc concentrations ($< \sim 0.25$ at.%) and Si less than 1.5 at.% is delineated by dashed lines, which means the solvus curves are not well studied. There are articles [25–27,30] stating that Si may decrease an alloy's microhardness because of its tendency to form the V-phase, and hence the Si concentration should be maintained at a value less than 0.15 at.% [25,27]. The alloys discussed in the literature all have Si concentrations greater than the values we studied (considering Si to be an alloying element and not an impurity). Alternatively, Zakharov [26,27] and Røyset et al. [31] investigated Al–0.24 at.% Sc with Si additions varying from 0 to about 0.8 at.%; the smallest concentrations studied, besides 0 at.%, were 0.05 at.% by Zakharov and 0.2 at.% by Røyset. Silicon additions decrease the Sc solubility in $\alpha$-Al (agreed on by Zakharov and Røyset) and accelerate the $Al_3Sc$ precipitation kinetics (stated by Røyset, which contradicts Zakharov's results). The two later results agree with our findings. In Zakharov's and Røyset's research the aging treatments were performed, however, on as-cast samples having a Sc concentration of 0.24 at.% and not on homogenized ones having a Sc concentration <0.11 at.%. Therefore, both contained some primary $Al_3Sc$ precipitates in their specimens prior to the ageing treatment and hence they did not obtain large $N_v$ values and concomitantly larger microhardness values as a result of the Si additions.

The only reported measurement, to our knowledge, that was performed with an alloy having Sc and Si concentrations comparable to our work was performed by Du et al. [19]; CP-Al alloy with ~1000 at. ppc Sc and ~500 at. ppm Si. As noted, Section 3.5, this alloy was quenched immediately after solidification and then aged at 300 °C for up to 45 h, which is different from the thermal processing procedure we employed. The peak microhardness Du et al. measured was 650 MPa, which is in excellent agreement with the value of 642 MPa we measured for the alloy containing 1085 at. ppm Sc.

Du et al.'s [19] three-dimensional atom-probe measurements suggested that the Si atoms co-precipitate with the Sc atoms at the onset of precipitation. Additionally, based on their experimental observations, and density functional theory (DFT) calculations, Du et al. state that energetically the Si atoms prefer the Al sublattice sites of $Al_3Sc$ (L1$_2$), and that the stoichiometric formula is $(Al,Si)_3Sc$. Du et al. do not, however, consider the possible effect of Si on the precipitation kinetics.

Another possible explanation for the faster kinetics and larger microhardness values of the alloys containing Si is the existence of an attractive binding energy between Si atoms and vacancies (see values calculated from first-principles in Refs. [11] and [32]), where vacancies form clusters with Si atoms, which act as heterogeneous nucleation sites for $Al_3Sc$. This behavior, accelerating precipitation kinetics in aluminum alloys, due to the addition of Si, is also common in Al-TM alloys (TM = transition metal), as was found, for example, in Al–Ti–Si [33], in Al–Hf–Si [34], Al–Cu–Si [35,36] and Al–Zr–Si alloys [37–41]. For all these alloys, the accelerated precipitation kinetics was assumed to be caused by this suggested mechanism. This explanation is consistent with Du et al.'s findings [19] of the congruence of the Si and Sc concentration profiles within the precipitates, having a higher concentration values in the center of the precipitates, which decrease toward their peripheries.

Alternatively, there are two possible explanations assuming homogeneous nucleation. One, consistent with Zakharov's [26] and Røyset et al.'s [31] findings, is that the Si decreases the Sc solubility in $\alpha$-Al, and hence increases the thermodynamic driving force for precipitation. The other one is that the presence of Si decreases the $\alpha$-Al/Al$_3$Sc interfacial free energy due to interfacial segregation, which concomitantly decreases the critical radius for homogeneous nucleation. In general it is, however, difficult to achieve homogeneous nucleation even in simpler alloys: see, for example, Stowell's [42] criticism of Lesgoues' and Aaronson's research [43,44] on homogeneous nucleation of precipitates in the Cu–Co system.

### 4.2. Temporal evolution of precipitates

There are several mean-field models for describing Ostwald ripening (coarsening) for dilute binary alloys [45–48] as well as for ternary and multi-component alloys [49–53]. In our alloys the RE and Fe solutes are precipitating in $Al_3(Fe,RE)$ micrometer-scale precipitates, their concentrations in the $\alpha$-Al matrix are smaller than their initially small concentrations, and it can therefore be assumed that the $\alpha$-Al matrix does not contain RE and Fe solutes. Since the Si and AlH peaks overlap in the mass spectrum (Section 3.5), it is difficult to state with certainty whether the Si concentration in the $Al_3Sc$ precipitates is small or not. Hence, having no additional data, we are neglecting the Si in the temporal evolution calculations. We, therefore, use a first-order approximation and analyze the data as a pseudo-binary Al–Sc alloy. And because the Sc concentration is small it is a dilute solid solution. Using Calderon et al.'s modified LSW model for binary alloys [54] the following equation obtains for the Sc supersaturation:

$$\left\langle C_{Sc}^{Al,ff}(t) \right\rangle - \left\langle C_{Sc}^{Al,ff}(\infty) \right\rangle = \kappa_{Sc} t^{-1/3} \tag{3}$$
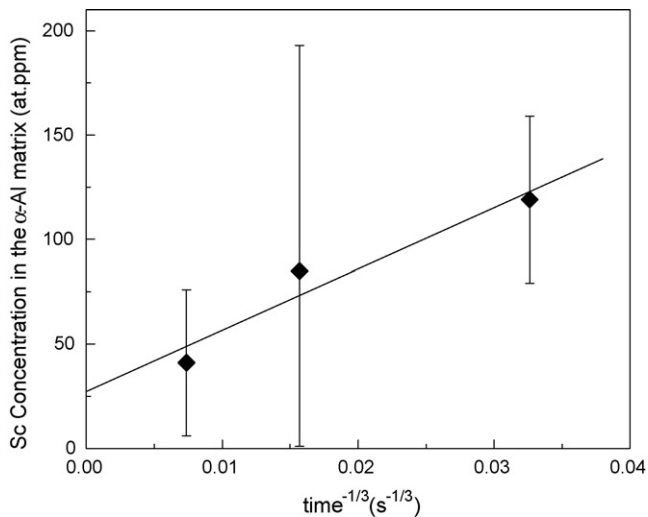
**Fig. 11.** The far-field Sc α-Al matrix concentration, $\left\langle C_{Sc}^{Al,ff}(t) \right\rangle$, versus $t^{-1/3}$ (data from Table 3). The error bars are due to counting statistics.

where $\left\langle C_{Sc}^{Al,ff}(t) \right\rangle$ is the Sc concentration in the far-field α-Al matrix, $\left\langle C_{Sc}^{Al,ff}(\infty) \right\rangle$ its equilibrium concentration in the far-field α-Al matrix as time $t \to \infty$, and $\kappa_{Sc}$ is the Calderon et al. coarsening rate constant. Based on the data listed in Table 3, a graph of $\left\langle C_{Sc}^{Al,ff}(t) \right\rangle$ versus $t^{-1/3}$ is presented in Fig. 11. A linear fit to the data yields a $\left\langle C_{Sc}^{Al,ff}(\infty) \right\rangle$ value of ~27 ± 8 at. ppm Sc with $\kappa_{Sc} = 2.95 \pm 0.35 \times 10^3$ (at. ppm) × (s)$^{1/3}$. Jo and Fujikawa [55], using electrical resistivity measurements, evaluated $\left\langle C_{Sc}^{Al,ff}(\infty) \right\rangle$ at temperatures between 370 and 460 °C for an Al–Sc (1500 at. ppm Sc) alloy. Extrapolating the Jo and Fujikawa data to 300 °C yields a $C_{Sc}^{Al,ff}(\infty)$ value of 15 at. ppm Sc, which is in approximate agreement with our results considering the statistical errors associated with our data and the extrapolation of their data.

In general, it is also possible to calculate the temporal evolution of the quantities $N_v(t)$ and $\langle R(t) \rangle$ [50,54]. To determine these dependences it requires, however, a change in the $\langle R(t) \rangle$ and $N_v(t)$ values of one order of magnitude, which is not the case for our data because of the coarsening resistance exhibited by the precipitates, Fig. 8.

## 5. Conclusions

We investigated the differences in the ageing behavior of high-purity Al (HP-Al) and commercial purity aluminum (CP-Al), whose major impurities are ~250 at. ppm Si and ~130 at. ppm Fe, alloyed with small concentrations of Sc and RE (~250 to ~1100 at. ppm Sc and ~50 at. ppm RE). The as-cast alloys are initially homogenized at 640 °C for 5–7 days and then aged at 300 °C for times up to 1 month. The micro- and nano-structures, as well as precipitation kinetics and basic mechanical properties, were studied. The main results and conclusions are:

1. For both types of aluminum, HP-Al and CP-Al, as the Sc concentration increases, the precipitation kinetics increase and concomitantly the peak microhardness values increase.
2. For CP-Al and HP-Al alloyed with the same Sc concentration, CP-Al has faster precipitation kinetics and a greater peak microhardness value. This result is technologically important because it demonstrates that it is possible to obtain better mechani-

cal properties by using the less expensive CP-Al alloyed with a smaller Sc concentration instead of the more expensive HP-Al alloyed with a larger Sc concentration. The precipitates in CP-Al exhibit strong coarsening resistance behavior.
3. Micrometer-scale Al$_{\sim3}$(Fe,RE) precipitates are detected in the homogenized alloy, which is quenched to room temperature. Hence, both Fe and RE solutes, have no effect on the precipitation kinetics and morphology of the nanometer-scale Al$_3$Sc precipitates and therefore no effect on the mechanical properties.
4. The main cause for the difference between the behavior of the CP-Al and the HP-Al alloys is the Si content. Silicon increases the Al$_3$Sc precipitation kinetics, increases the number density value, $N_v$, and hence results in higher peak microhardness values than HP-Al having the same Sc concentration.
5. The Sc equilibrium solubility in the α-Al matrix at 300 °C is estimated to ~27 ± 8 at. ppm Sc, which is in reasonable agreement with the extrapolation of prior resistivity data yielding a value of 15 at. ppm Sc.
6. The main room temperature strengthening mechanism in CP-Al and HP-Al alloys is the Orowan dislocation looping mechanism, where the dislocations bypass coherent precipitates due to the elastic stress fields associated with them.

## References

[1] M.Ye. Drits, L.B. Ber, Yu.G. Bykov, L.S. Toropova, G.K. Anastas'eva, Phys. Met. Metall. 57 (6) (1984) 118–126.
[2] J. Røyset, N. Ryum, Int. Mater. Rev. 50 (1) (2005) 19–44.
[3] Y. Harada, D.C. Dunand, Mater. Sci. Eng. A 329–331 (2002) 686–695.
[4] JCPDS-International Center for Diffraction Data, 1998.
[5] Y. Harada, D.C. Dunand, Scripta Mater. 48 (3) (2003) 219–222.
[6] D.N. Seidman, Ann. Rev. Mater. Res. 37 (2007) 127–158.
[7] C.B. Fuller, D.N. Seidman, D.C. Dunand, Acta Mater. 51 (16) (2003) 4803–4814.
[8] M.E. Van Dalen, T. Gyger, D.C. Dunand, D.N. Seidman, Microsc. Microanal. 13 (2007) 1618–1619.
[9] R.A. Karnesky, D.N. Seidman, D.C. Dunand, Mater. Sci. Forum 518–521 (2006) 1035–1040.
[10] R.A. Karnesky, M.E. van Dalen, D.C. Dunand, D.N. Seidman, Scripta Mater. 55 (2006) 437–440.
[11] C. Wolverton, Acta Mater. 53 (2007) 5867–5872.
[12] S.I. Fujikawa, M. Sugaya, H. Takei, K. Hirano, J. Less-Common Met. 63 (1979) 87–97.
[13] M. Ocko, E. Babic, R. Krsmik, E. Girt, B. Leontic, J. Phys. F 6 (1976) 703–707.
[14] D.R. Lide (Ed.), CRC Handbook of Chemistry and Physics, 83rd ed., CRC Press LLC, Florida, 2003.
[15] O.C. Hellman, J.A. Vandenbroucke, J. Rüsing, D. Isheim, D.N. Seidman, Microsc. Microanal. 6 (2000) 437–444.
[16] K.E. Yoon, R.D. Noebe, O.C. Hellman, D.N. Seidman, Surf. Interface Anal. 36 (2004) 594–597.
[17] C.B. Fuller, J.L. Murray, D.N. Seidman, Acta Mater. 53 (2005) 5401–5413.
[18] C.B. Fuller, D.N. Seidman, Acta Mater. 53 (2005) 5415–5428.
[19] G. Du, J. Deng, Y. Wang, D. Yan, L. Rong, Scripta Mater. 61 (2009) 532–535.
[20] E.A. Marquis, D.N. Seidman, D.C. Dunand, Acta Mater. 51 (2003) 4751–4760.
[21] P.B. Hirsch, F.J. Humphreys, in: A. Argon (Ed.), Physics and Strength of Plasticity, MIT Press, Cambridge, MA, 1969, pp. 189–216.
[22] P.W. Martin, Precipitation Hardening, Butterworth–Heinemann, London, 1998.
[23] L.M. Brown, R.K. Ham, in: A. Kelly, R.B. Nicholson (Eds.), Strengthening Methods in Crystals, Elsevier, London, 1971, pp. 9–135.
[24] D. Tabor, Br. J. Appl. Phys. 7 (1956) 159–166.
[25] V.G. Davydov, T.D. Rostova, V.V. Zakharov, Yu.A. Filatov, V.I. Yelagin, Mater. Sci. Eng. A 280 (2000) 30–36.
[26] V.V. Zakharov, Met. Sci. Heat Treat. 39 (1–2) (1997) 61–66.
[27] V.V. Zakharov, T.D. Rostova, Met. Sci. Heat Treat. 49 (9–10) (2007) 435–442, (Translated from Metallovedenie i Termicheskaya Obrabotka Metallov 9 (2007) 12–19).

[28] V.I. Elagin, V.V. Zakharov, T.D. Rostova, UDC 669.715′793 (Translated from Metallovedenie i Termicheskaya Obrabotka Metallov 1 (1992) 24–28).

[29] L.L. Rokhlin, T.V. Dobhatkina, M.L. Kharakterova, Powder Metall. Met. Ceram. 36 (3–4) (1997) 128–132.

[30] M.L. Kharakterova, D.G. Eskin, L.S. Toropova, Acta Metall. 42 (7) (1994) 2285–2290.

[31] J. Røyset, H. Hovland, N. Ryum, Mater. Sci. Forum 396–402 (2002) 619–624.

[32] D. Simonovic, M.H.F. Sluiter, Phys. Rev. B 79 (2009) 054304, 1–12.

[33] P. Malek, M. Janecek, B. Smola, Metallic Mater. 38 (3) (2000) 113–122.

[34] S. Hori, N. Furushiro, W. Fujitani, J. Jpn. Inst. Light Met. 31 (10) (1981) 649–654.

[35] D. Mitlin, V. Radmilovic, J.W. Morris Jr., Metall. Mater. Trans. A 31 (2000) 2697–2711.

[36] A.J. Perry, K.M. Entwistl, Phil. Mag. 18 (1968) 1085–1088.

[37] T. Sato, A. Kamio, G.W. Lorimer, Mater. Sci. Forum 217–222 (1996) 895–900.

[38] T. Ohashi, R. Ichikawa, J. Jpn. Inst. Met. 34 (6) (1970) 604–610.

[39] S. Hori, T. Kondo, S. Ikeno, J. Jpn. Inst. Light Met. 28 (2) (1978) 79–84.

[40] H. Westengen, O. Reiso, L. Auran, Aluminium 56 (1980) 768–775.

[41] B. Forbord, H. Hallem, K. Marthinsen, Proceedings of the 9th International Conference on Aluminium Alloys (ICAA9), 2004, pp. 1179–1185.

[42] M.J. Stowell, Mater. Sci. Technol. 18 (2) (2002) 139–144.

[43] H.I. Aaronson, F.K. Legoues, Metall. Trans. A 23 (1992) 1915–1945.

[44] F.K. Legoues, H.I. Aaronson, Acta Metall. 32 (1984) 1855–1864.

[45] I.M. Lifshitz, V.V. Slyozov, J. Phys. Chem. Solids 19 (1961) 35–50.

[46] C. Wagner, Electrochem. Z 65 (1961) 581–591.

[47] A.J. Ardell, Acta Metall. 15 (1967) 1772–1775.

[48] A.J. Ardell, Acta Metall. 20 (1972) 61–71.

[49] A. Umantsev, G.B. Olson, Scripta Metall. 29 (1993) 905–908.

[50] C.J. Kuehmann, P.W. Voorhees, Metall. Mater. Trans. A 27 (1996) 937–943.

[51] C.K. Sudbrack, K.E. Yoon, R.D. Noebe, D.N. Seidman, Acta Mater. 54 (2006) 3199–3210.

[52] C.K. Sudbrack, R.D. Noebe, D.N. Seidman, Acta Mater. 55 (2007) 119–130.

[53] C. Booth-Morrison, J. Weninger, C.K. Sudbrack, Z. Mao, R.D. Noebe, D.N. Seidman, Acta Mater. 56 (14) (2008) 3422–3438.

[54] H.A. Calderon, P.W. Voorhees, J.L. Murray, G. Kostorz, Acta Metall. Mater. 42 (3) (1994) 991–1000.

[55] H.H. Jo, S.I. Fujikawa, Mater. Sci. Eng. A 171 (1993) 151–161.